Main Group Chemistry

Effects of Ce doping on the structural, optical and electrical properties of spinel SrCo2O4 thin films

Journal:	*Main Group Chemistry*
Manuscript ID	MGC-25-0035.R2
Manuscript Type:	Original Research Article
Date Submitted by the Author:	21-Dec-2025
Complete List of Authors:	Hireche, khaoula; Ibn Khadoun University Tiaret Faculty of Material Sciences, Physics ABDELMALEK, KHARROUBI; Ibn Khadoun University Tiaret Faculty of Material Sciences, Physics Benhebal, Hadj; Ibn Khadoun University Tiaret Faculty of Material Sciences, Chemistry Benrabah, Bedhiaf; Ibn Khadoun University Tiaret Faculty of Material Sciences Touati, Mohamed.; Ibn Khadoun University Tiaret Faculty of Material Sciences Lambert, Stephanie; Universite de Liege Faculte des Sciences, Department of Chemical Engineering – Nanomaterials, mahy, julien; University of Liege Faculty of Sciences, Department of Chemical Engineering – Nanomaterials, Catalysis & Electrochemistry,
Keywords:	SrCo2O4, Thin films, Ce-doping, Sol-Gel, Dip-Coating
Abstract:	Cerium-doped strontium cobaltite spinel ($SrCo_2O_4$) thin films were synthesized using a sol–gel dip process and subsequently deposited onto glass substrates by a coating technique. The influence of Ce doping on structural, optical and electrical properties has been studied using X-ray diffraction (XRD), Fourier-transform infrared spectroscopy (FTIR), UV–Vis spectrophotometry and impedance spectroscopy. The XRD analysis indicates that all samples exhibit a single-phase cubic spinel structure assigned to the Fd3m space group, with the (311) plane emerging as the dominant orientation. IR spectra revealed the presence of vibrational modes associated to spinel SrCo2O4. Deposited thin films show average transmittance above 80% in the visible range. The impedance measurements show that the equivalent circuit of the diagram of Ce doped SrCo2O4 layers is an RpCp parallel. when the resistance Rp decreases while the capacitance Cp increases with Ce doping. Cerium incorporation alters the structural, optical, and electrical characteristics of $SrCo_2O_4$, leading to an increase in average crystallite size to 27.93 nm, a decrease in the optical band gap to 1.40 eV, a reduction in resistance to 33.06 Ω, and an enhancement in capacitance to 7.32 nF at a doping level of 5%.

Note: The following files were submitted by the author for peer review, but cannot be converted to PDF. You must view these files (e.g. movies) online.
Figure.jpg.zip

Effects of Ce doping on the structural, optical and electrical properties of spinel $SrCo_2O_4$ thin films

Effects of Ce doping on the structural, optical and electrical properties of spinel $SrCo_2O_4$ thin films

Abdelmalek Kharroubi*[1], Hireche Khaoula[1],Hadj Benhebal[2], Bedhiaf Benrabah[1], Touati Mohamed[1], Stéphanie D. Lambert[3] and Julien G. Mahy[3]

Laboratory of Physical Engineering Faculty of Mater Sciences, University Ibn Khaldoun Tiaret, Algeria

[2]Department of Chemstryl, Faculty of Mater Sciences, University Ibn Khaldoun Tiaret, Algeria
3Department of Chemical Engineering – Nanomaterials, Catalysis & Electrochemistry, University of Liège, Belgium.

Corresponding author: abdelmalek.kharroubi@univ-tiaret.dz

Abstract:

Cerium-doped strontium cobaltite spinel ($SrCo_2O_4$) thin films were synthesized using a sol–gel dip process and subsequently deposited onto glass substrates by a coating technique. The influence of Ce doping on structural, optical and electrical properties has been studied using X-ray diffraction (XRD), Fourier-transform infrared spectroscopy (FTIR), UV–Vis spectrophotometry and impedance spectroscopy. The XRD analysis indicates that all samples exhibit a single-phase cubic spinel structure assigned to the Fd3m space group, with the (311) plane emerging as the dominant orientation. IR spectra revealed the presence of vibrational modes associated to spinel $SrCo_2O_4$. Deposited thin films show average transmittance above 80% in the visible range. The impedance measurements show that the equivalent circuit of the diagram of Ce doped $SrCo_2O_4$ layers is an RpCp parallel. when the resistance Rp decreases while the capacitance Cp increases with Ce doping. Cerium incorporation alters the structural, optical, and electrical characteristics of $SrCo_2O_4$, leading to an increase in average crystallite size to 27.93 nm, a decrease in the optical band gap to 1.40 eV, a reduction in resistance to 33.06 Ω, and an enhancement in capacitance to 7.32 nF at a doping level of 5%.

Keywords: $SrCo_2O_4$, Thin films, Doping, Sol-Gel, Dip-Coating.

1. Introduction:

Faced with a critical energy situation in today's world, research has increased in order to develop functional materials with low size, cost and environmental impact. In this context, structured nanomaterials based on oxide semiconductors are essential for the development of devices for the production, conversion and storage of energy [1,2]. Among semiconducting metal oxides, spinel-type continues to fascinate researchers with their exceptional optical, electrical, mechanical, magnetic, elastic, and structural properties, leading to the prospect of extensive exploitation and therefore potential applications in many areas of technology, including optoelectronics devices [3-10]. Spinels constitute a large family of mixed oxides whose generic formula is AB_2O_4, with A and B being metal cations with oxidation states 2 and 3, respectively [11]. Among transition metal oxides, substituted products of cobalt cobaltite (Co_3O_4) with general formula MCo_2O_4 (M = Ni, Cu, Zn, Mn, Mg, Cd, etc.) are an important group of materials which have given extensive interest for electrochemical applications, especially for

batteries, supercapacitors, and electrocatalysis, owing to their particular structural, optical and electrical properties [12-17]. Doping with metallic and non-metallic elements could further contribute to the design and manufacturing of materials with improved morphological and optoelectronic properties [16]. Several metallic dopants have been added to the antiferromagnetic p-type transparent semiconductor Co_3O_4 for the improvement of its electrochemical stability like: Sb, Cr, Ni, Cu, Zn, Sn, Mg, Mo, Fe, Ag, etc. Indeed, the presence of two metal cations with mixed valences facilitates electron transport with relatively low activation energy [18-26]. Because cerium exhibits multiple oxidation states such as Ce^{3+} and Ce^{4+}, it can be used as a dopant to improve the electrochemical properties of many nanostructured materials [27,28]. The choice of an appropriate preparation method has a significant impact on the properties and applications of thin films [29]. Number of synthesis methods is known to prepare thin films of cobalt-based spinel oxides such as: thermal decomposition [30], spray pyrolysis [31], microwave [32], radio-frequency magnetron sputtering [33], pulsed laser deposition [34] and sol-gel dip-coating [35-37]. The sol-gel dip-coating method offers benefits such as speed, simplicity in fabrication, excellent reproducibility and film uniformity [38]. However, the homogeneity and properties of the films obtained by this method depend on a number of factors, notably the solubility of the coating components used as well as the concentration and viscosity gradients induced by evaporation as a function of time in the solution [39,40]. In the present work, three oxides pure $SrCo_2O_4$ and Ce-doped $SrCo_2O_4$ at 3 and 5%, were deposited on pyrex glass by dip coating process at room temperature and their structural, morphological, optical and electrical properties were investigated.

2. Experimental details

Ce-doped spinel $SrCo_2O_4$ thin films were deposited on cleaned Pyrex glass substrates using the sol–gel dip-coating method. The first precursor solution was prepared by dissolving 2.91 g of cobalt nitrate ($Co(NO_3)_2 \cdot 6H_2O$) (Sigma Aldrich, 99.8%) in 120 mL of ethanol (C_2H_6O) (Sigma Aldrich, 99.8%). Magnetic stirring for 30 min yielded a uniformly colored solution. The second precursor, a strontium nitrate solution, was obtained by dissolving 4.36 g of $Sr(NO_3)_2$ in 120 mL of ethanol. After blending both solutions, citric acid (Sigma Aldrich, 99.5%) was added. The mixture was then slowly heated to 80 °C and maintained under magnetic stirring for 5 h, forming a purple-red sol.

Cerium precursor solutions were prepared by dissolving 0.2 g of $Ce(NO_3)_3 \cdot 6H_2O$ (Sigma Aldrich, 99.9%) in ethanol and stirring for 2 h, producing a clear and slightly viscous solution.

The prepared sols were loaded into the dip-coating system. Depositions were performed as single-layer coatings onto well-cleaned Pyrex glass slides (25 mm × 75 mm × 1 mm) at room temperature, under 40% relative humidity, and at a withdrawal speed of 50 mm/min. Three films were prepared: one undoped $SrCo_2O_4$ and two Ce-doped $SrCo_2O_4$ films containing 3% and 5% Ce. The dip-coated layers were dried at 100 °C for 20 min and subsequently annealed at 500 °C. The complete procedure is summarized in Fig (1).

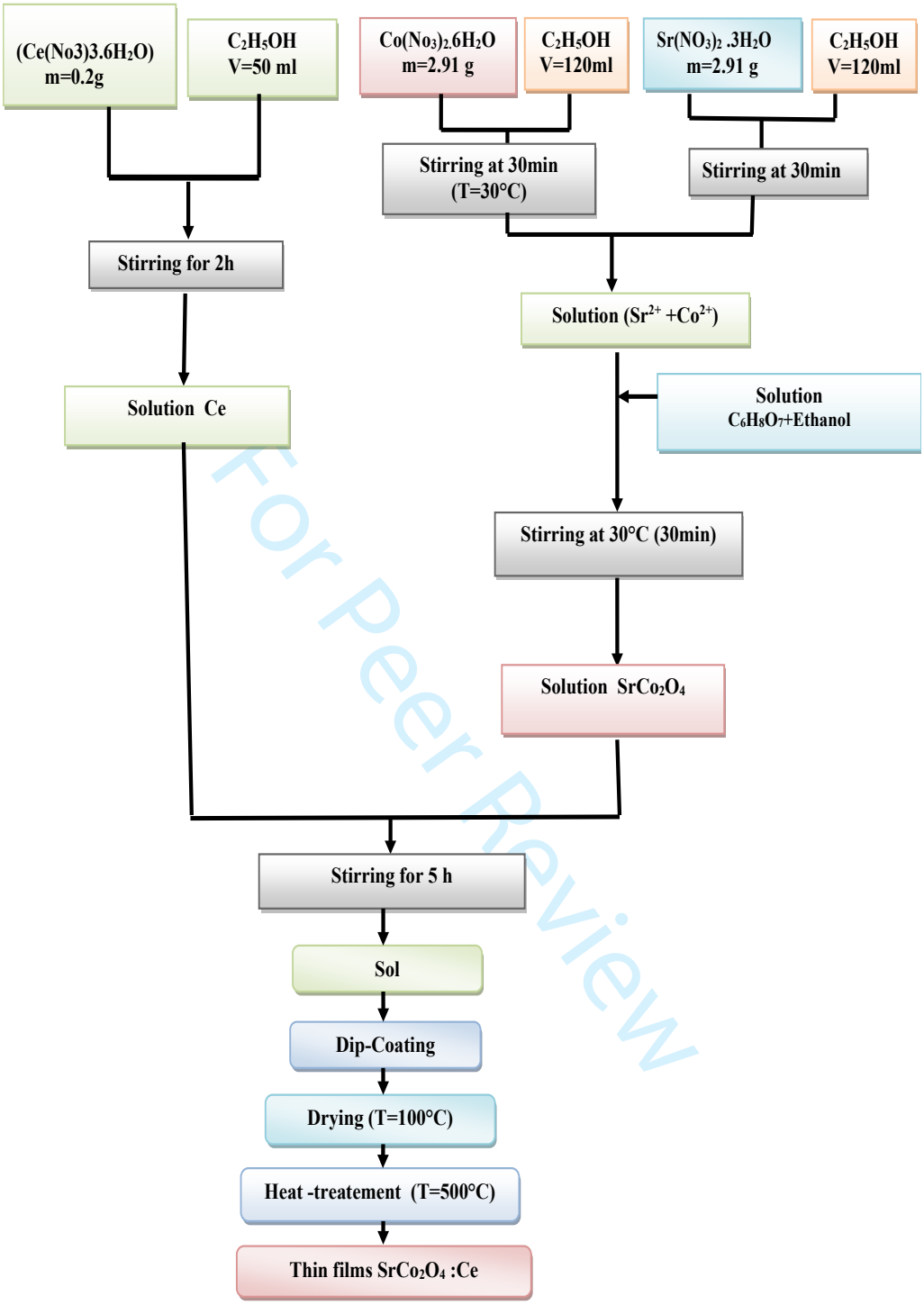

Fig 1. The sol–gel dip-coating process for fabricating Ce-doped $SrCo_2O_4$ thin films

3. Characterizations

The prepared thin films of $SrCo_2O_4$ and Ce-doped $SrCo_2O_4$ were characterized by carrying out structural, optical and electrical studies. The X-ray diffraction pattern of the prepared samples was collected by using a Rigaku miniflex 600 X-ray diffractometer with Cu-Kα line (λ=1.5406Å) in a wide range of 2θ, i.e., from 0° to 80°.

The FTIR spectrum was recorded on the Shimadzu 8400 FTIR spectrophotometer from 400 cm^{-1} to 4000 cm^{-1}. Optical properties from UV–Vis spectroscopic studies were obtained by using the Shimadzu 1650 UV–Vis spectrophotometer. Finally, the analysis by complex impedance spectroscopy was carried in the frequency range 75 kHz to 20 MHz with oscillation amplitude of 1 V using Agilent 4284A LCR-meter.

4. Results and discussion

4.1. Structural characterization

The phase and crystal structure information of the $SrCo_2O_4$ and Ce-doped $SrCo_2O_4$ thin films were studied using XRD as displayed in Fig. For the $SrCo_2O_4$ thin film, the diffraction peaks at 2θ = 18.81, 31.13, 36,61, 38.23, 44.49, 55.19, 59.19, 65.07, 68.45 and 73.55 are corresponds to (111), (220), (311), (222), (400), (422), (511), (440), (531), (620) planes, respectively. The ten diffraction peaks recorded can be well indexed with the cubic spinel structure (space group of Fd-3m) of Co_3O_4 (JCPDS no. 42-1467) [41-42]. No new diffraction peaks on the diffractograms of the doped samples confirming the formation of single-phase spinel cubic structure and indicating that Ce was substituted into the crystal lattice of strontium cobalt oxide.

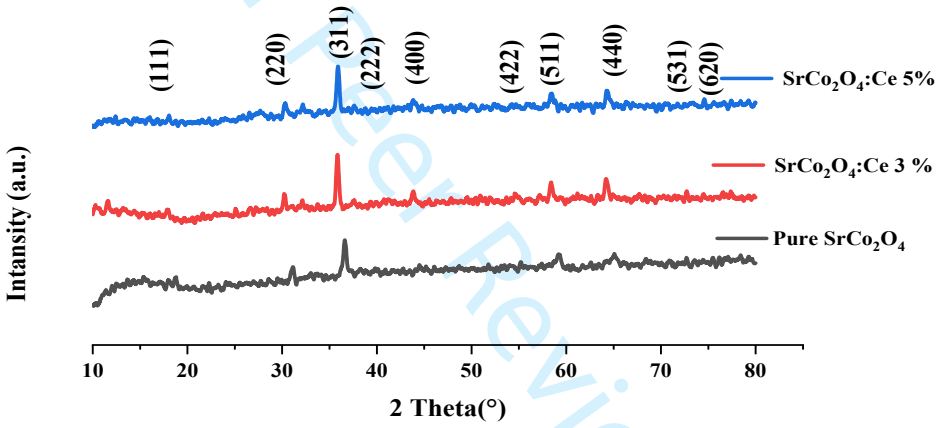

Fig. 2. XRay diffraction pattern for $SrCo_2O_4$ and Ce-doped $SrCo_2O_4$

In addition to the average crystallite size (D), d spacing, lattice constant (a), and unit cell volume (V_{cell}) of thin films were calculated from the most intense (311) plane of the samples using the following equation[43-44].

$$D = \frac{k\lambda}{\beta cos\theta} \quad \text{..... (1)}$$

Where β is full width at half maximum of intense peak, θ is the Bragg angle of the intense crystallographic plane, *k* is a constant (0.9) and λ = 1.5406 Å.

$$a = d_{hkl}\sqrt{h^2 + k^2 + l^2} \quad \text{..... (2)}$$

$$V_{cell} = a^3 \text{..... (3)}$$

The elastic deformation of thin films, which contributes to peak broadening, can be estimated by using the formula [45]]:

$$\delta = 1/D^2 \quad \text{..... (4)}$$

The microstrain and dislocation density of thin films are calculated from the following equations[46]

$$\varepsilon = \beta\cos\theta/4 \quad \text{..... (5)}$$

Table .1. Structural parameters as crystalline size, lattice parameter, cell volume, micro strain and dislocation density of $SrCo_2O_4$ and Ce-doped $SrCo_2O_4$

Sample	Undoped $SrCo_2O_4$	$SrCo_2O_4$:Ce 3%	$SrCo_2O_4$:Ce 5%
B	0,0061928	0,0055822	0,0052333
Θ	18,305	18,42	18,44
cos θ	0,949398	0,94876577	0,9486554
Sinθ	0,314075	0,31598023	0,3163114
Average crystallite size D (nm)	23,58	26,18	27,93
d_{hkl} (Å)	2,453	2,438	2,435
Lattice constant a (Å)	8,136	8,086	8,076
Unit cell volume V_{cell} $(Å)^3$	538,56	528,69	526,73
Dislocation density δ (lines/m^2)	17,98 10^{14}	14,59 10^{14}	13,42 10^{14}
Microstrain ε ($line^{-2}$ m^{-4})	0,0014698	0,0013240	0,0012411

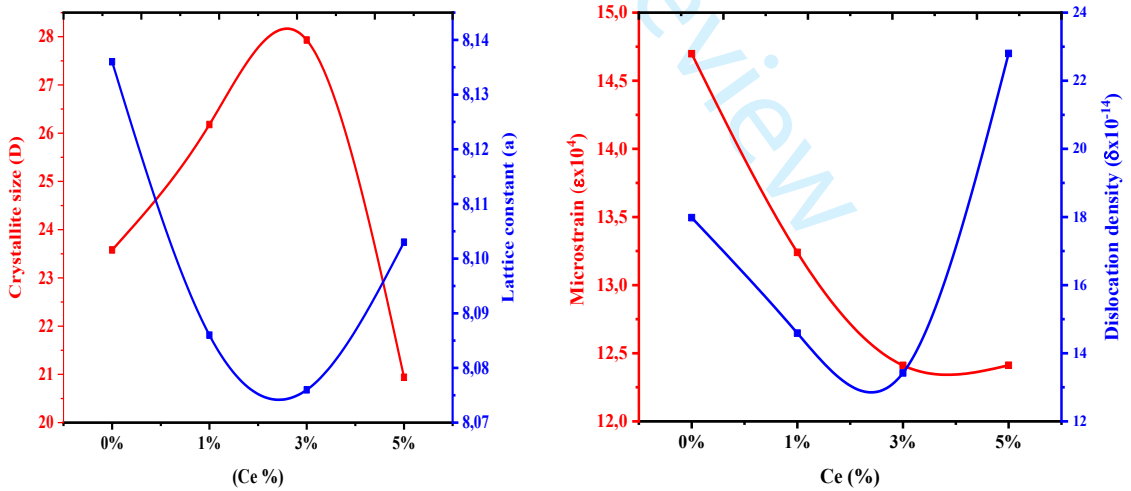

Fig. 3. Crystallite size, Microstrain and dislocation density variations for pure and Ce-doped $SrCo_2O_4$

The calculations gave the results recorded in Table 1. The results grouped in Table 1, show that the crystallite size of the samples increases while the dislocation density and lattice strain decrease for low Ce doping, then the opposite phenomenon is obtained with the increase in the doping rate.

4.2. Infrared spectroscopy

Infrared absorption spectra of the pure and doped $SrCo_2O_4$ are shown in Fig.4.Two strong peaks appeared for all the samples at 582 cm^{-1} and 661 cm^{-1} are respectively attributed to the M-O vibrations in the octahedral and tetrahedral sites of the AB_2O_4 spinel lattice [47], thus confirming the formation of $SrCo_2O_4$ material with a spinel structure. The peak at 1618 cm^{-1} and the broad band centered at about 3389 cm^{-1} are respectively assigned to the bending and stretching modes of the -OH groups of the adsorbed water [48]. The FTIR spectra of the doped samples are similar to that of the undoped sample, which illustrates the similar nature of the chemical bonds. The interaction between the cerium ions incorporated with the native strontium and cobalt ions can be deduced from the change in intensity of the peaks relating to the spinel structure (ie. the peaks at 582 cm^{-1} and 661 cm^{-1}) [49].

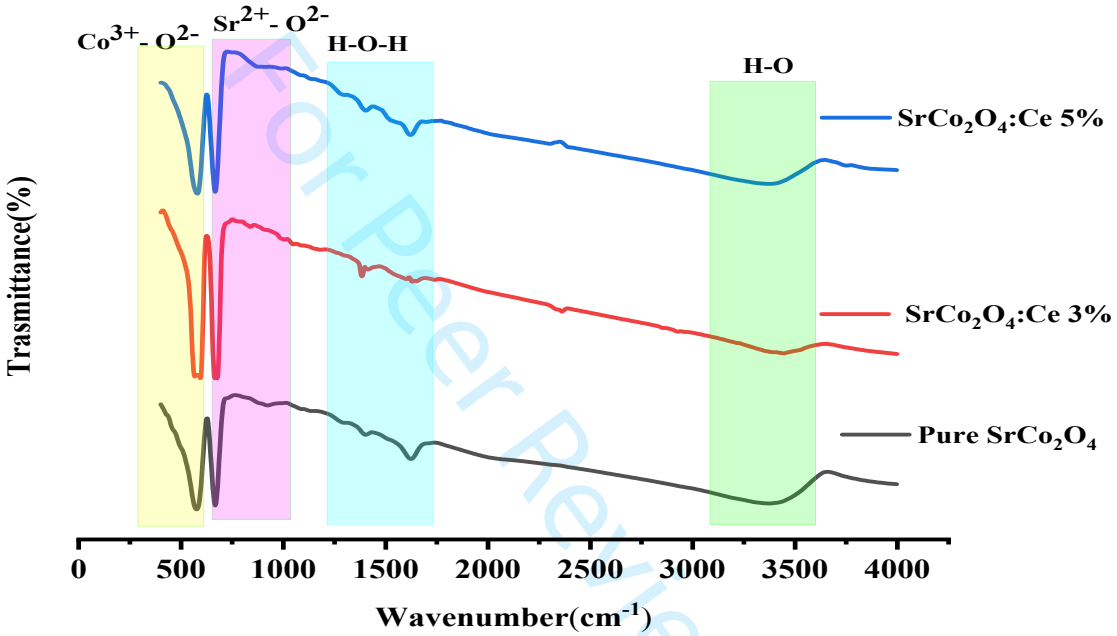

Fig.4. IR spectrum of pure and Ce-doped $SrCo_2O_4$

4.3. Optical characterisation

The influence of cerium doping concentration on the optical properties of $SrCo_2O_4$ thin films was studied by optical measurements. Fig.5.A illustrates the transmittance spectra of both undoped and Ce-doped films at different concentration within the wavelength range of 350-900 nm. All deposited films present a high transparency, the undoped $SrCo_2O_4$ films displayed an optical transmittance surpassing 80%. With increasing Ce doping levels, the transmittance values progressively improved, reaching values exceeding 80%. These differences in optical transmittance over the visible range are due to changes in crystallite size and surface roughness generated by Ce incorporation[50]. A similar behavior has been observed by Boudjouan, F et al, where enhanced crystalline quality was found to reduce light scattering from the grains constituting the film, thereby increasing its transparency[51].

Fig. 5.B depicts the UV-Vis absorption spectra of pure $SrCo_2O_4$ and Ce-$SrCo_2O_4$ thin film. This figure indicates that the undoped $SrCo_2O_4$ film exhibits higher absorbance compared to the doped ones. The decrease in absorbance observed in the doped samples may be attributed to defect states arising from lattice imperfections caused by the varying Ce concentrations and may also be linked to the

deterioration of crystallinity at higher doping levels[52].The absorbance spectra shown in Fig 5.C were also used to determine the optical band gap of the undoped $SrCo_2O_4$ and Ce-$SrCo_2O_4$ nanostructures. Tauc plots have been drawn for each nanostructure based on the Transmittance data, using the Tauc relation presented in the following equation:

$$(\alpha h\nu)^m = A^*(h\nu - Eg) \quad \text{..... (6)}$$

Here, α denotes the absorption coefficient, ν is the photon frequency, A is a constant, and h represents the photon energy. The exponent *m* takes the value 1/2 for an indirect allowed transition and 2 for a direct allowed electronic transition. The band-gap (Eg) values were obtained by extrapolating the linear region of the Tauc plot of $(\alpha h\nu)^2$ versus hν, as illustrated in Fig. 5.D, and the corresponding results are summarized in Table 2.

The direct upper bandgap value of Ce-doped SrCo2O4:Ce Thin Films was observed in the range of (1.76 - 1.70 eV). According to Table 2, it is observed that the bandgap continues to decrease with the increase in Ce content; this decrease may be due to the formation of sub-bands between the energy bandgap and the merging of their sub-bands with the conduction band to form a continuous band. This result has been obtained by several researchers who have doped different materials with cerium [53-55].

Compared to absorption behavior in strongly doped crystalline semiconductors, sub-bandgap absorption can be described by the Urbach law which relates to the characteristic distribution and width of band-tail states[56].Urbach tails generally develop in materials with low crystallinity, structural disorder, or amorphous character, as these states extend into the bandgap[57-58].

The relationship between the absorption coefficient (α) and photon energy (hν) in the low-photon-energy region follows the empirical Urbach rule, expressed as [59]:

$$\alpha = \alpha_0 \exp\left(\frac{h\nu}{E_u}\right) \quad \text{..... (7)}$$

$$\ln \alpha = \ln \alpha_0 + \left(\frac{h\nu}{E_u}\right) \quad \text{..... (8)}$$

Where α_0 is the pre-exponential factor, $(h\nu)$ the photon energy and E_u is the band tail width or disorder energy.

Hence, the Urbach energy $E_u$of the $SrCo_2O_4$ thin films may be estimated from the slope of the linear fit obtained by plotting ln(α) versus the incident photon energy (hν), as represented in Fig.6.

The lowest Urbach energy was obtained for the undoped $SrCo_2O_4$ film, indicating strong crystallinity and a low density of defects. However, the Urbach energy rose with doping, implying more structural disorder, which may be related to the growth of surface roughness. It can be observed from the data in Table 1 that the E_u values increase with the Ce doping level. This increased disorder correlates with a reduction in the optical band gap energy (Eg), in line with the well-established inverse relationship between bandgap energy and Urbach one in disordered semiconductors. Fig.7. shows this linear relationship between the band gap energy and the Urbach tail width which is consistent with previous reports and may be attributed to the reduction in grain size. In addition, the increase in Urbach energy can cause a narrowing of the band gap due to the extension of the band tails[60].

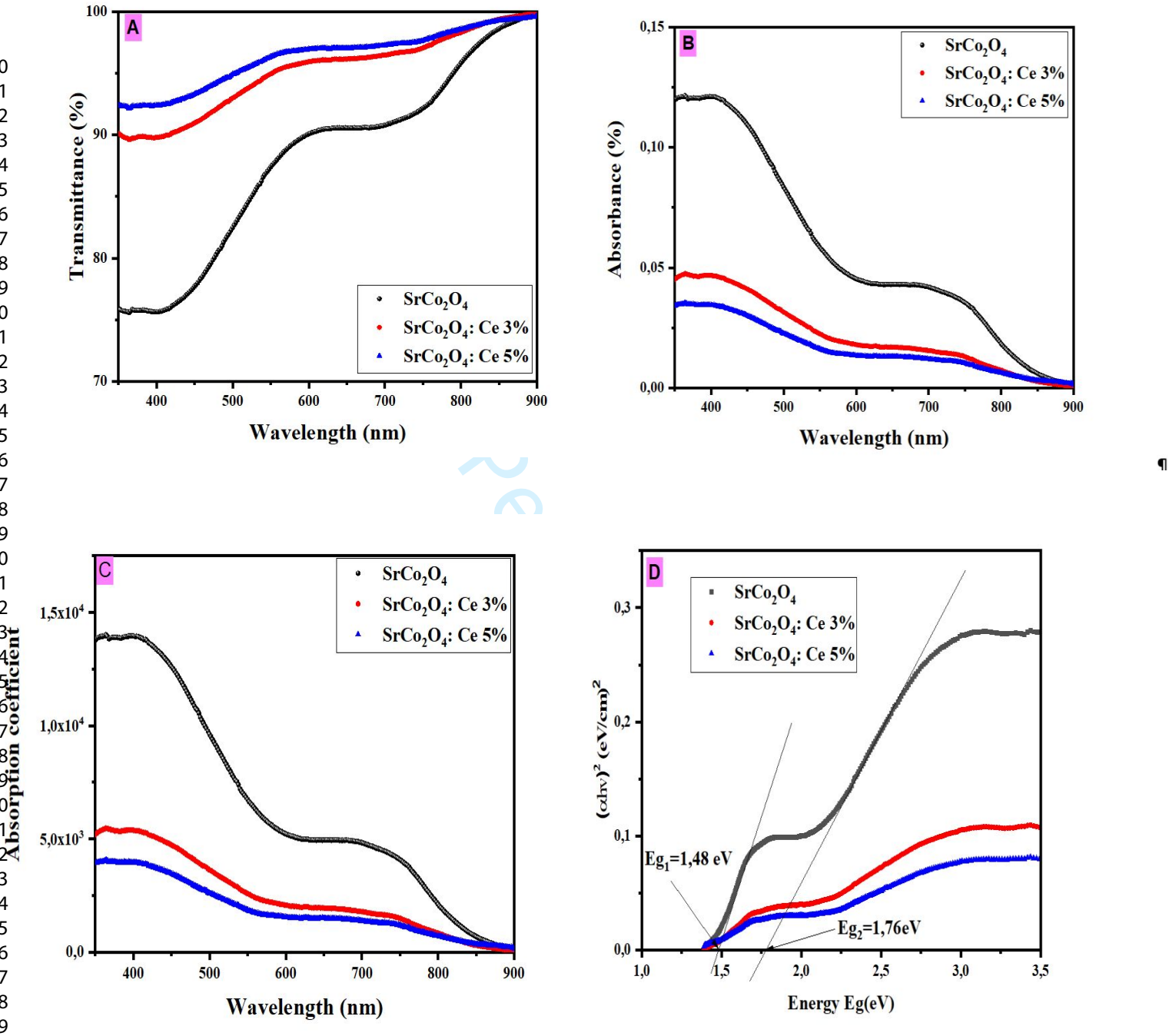

Fig. 5. (A) Transmittance, **(B)** Absorbance and **(C)** Absorption coefficient **(D)** Tauc plot of spectra of pure and Ce-doped $SrCo_2O_4$.

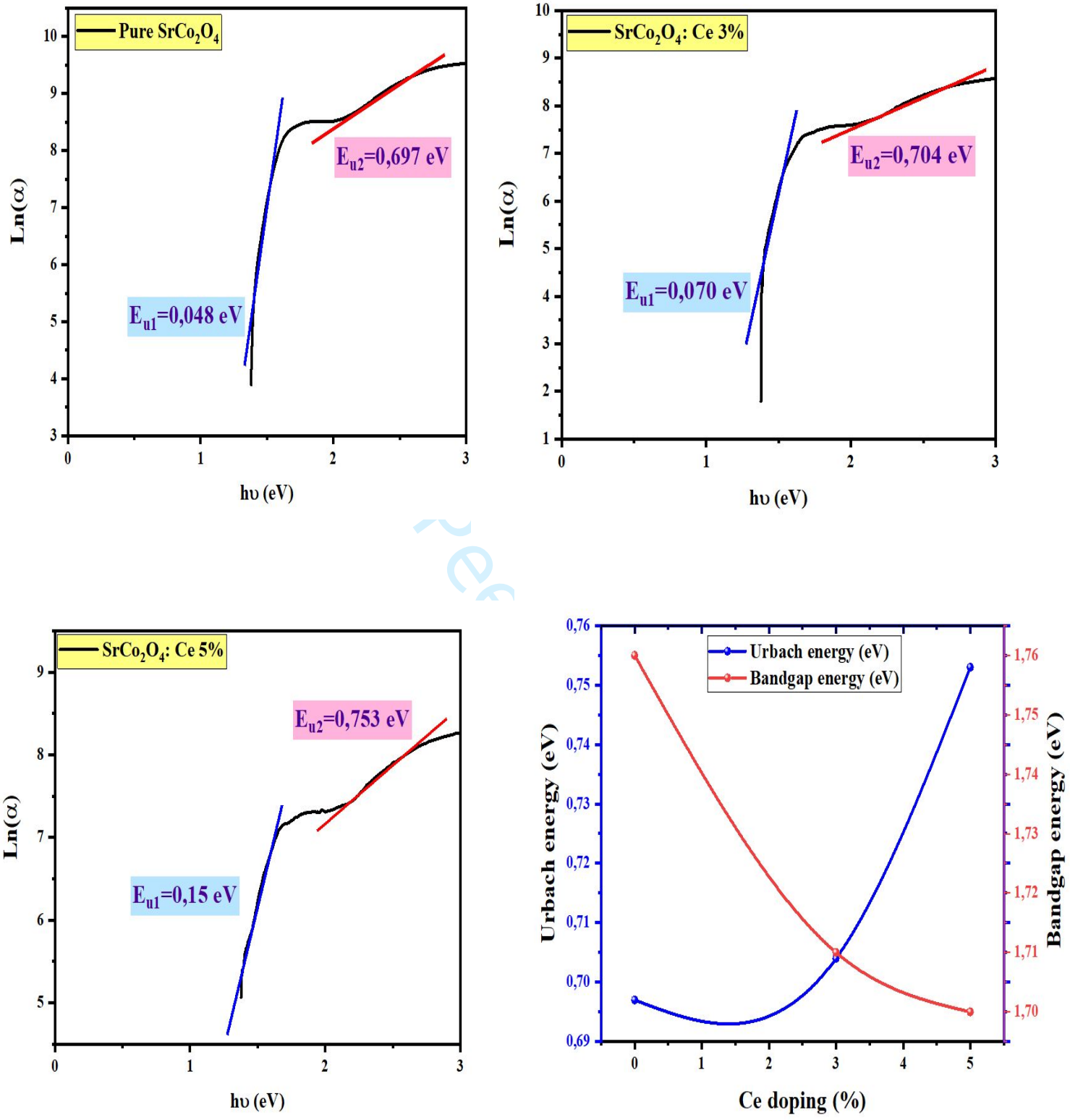

Fig.6 . Urbach energy of undoped and doped $SrCo_2O_4$ films with different percentage ratios of Ce

Fig. 7. The variation of optical band gap and.Urbach energy of pure and Ce dopedCo_2O_4 thin film

Table 2: The optical band gap and Urbach energy for the undoped and Ce-doped $SrCo_2O_4$ thin films.

Ce content at. %	Bandgap (eV)		Urbach energy (meV)	
	E_{g1} (eV)	E_{g2} (eV)	E_{u1} (meV)	E_{u2} (meV)
0	1,48	1.76	48	697
3	1,44	1.71	70	704
5	1,40	1.70	150	753

4.3.1. Refractive Index and Extinction Coefficient:

The refractive index (n) and other dispersion parameters play a crucial role in determining the electronic properties of semiconductor materials employed in optoelectronic devices[61]**.**

The refractive index (n) which fully describes how the material interacts with light, is related to the complex refractive index (n*) through the following relation[62]:

$$n^* = n + ik \quad \text{..... (9)}$$

Here, n indicate the real part of the complex refractive index, representing the extent to which light is retarded through the material. It is an important optical characteristic for solar cell absorber layers, while k is the imaginary part, also referred to as the extinction coefficient, it quantifies the attenuation of light within the material due to absorption or other inelastic scattering processes, such as the Compton effect, photoelectric effect, and pair production. The following relations contribute to determining the value of n and k, respectively[63]:

$$n = \frac{1+\sqrt{R}}{1-\sqrt{R}} \quad \text{..... (10)}$$

$$k = \frac{\alpha.\lambda}{4\pi} \quad \text{..... (11)}$$

Where R, α and λ are reflectance, absorption coefficient and incident wavelength, respectively.

The calculated refractive index spectra (n) and the extinction coefficient for the synthesized $SrCo_2O_4$ layers are shown in Fig.8. A and B. As we can see, a further increase in Ce content leads to a reduction in the refractive index, which is likely associated with defect formation and impurity incorporation in the thin films induced by Ce doping[61]. Materials with a low value of (n) are very suitable for SC absorber material and an antireflection layer. [65].

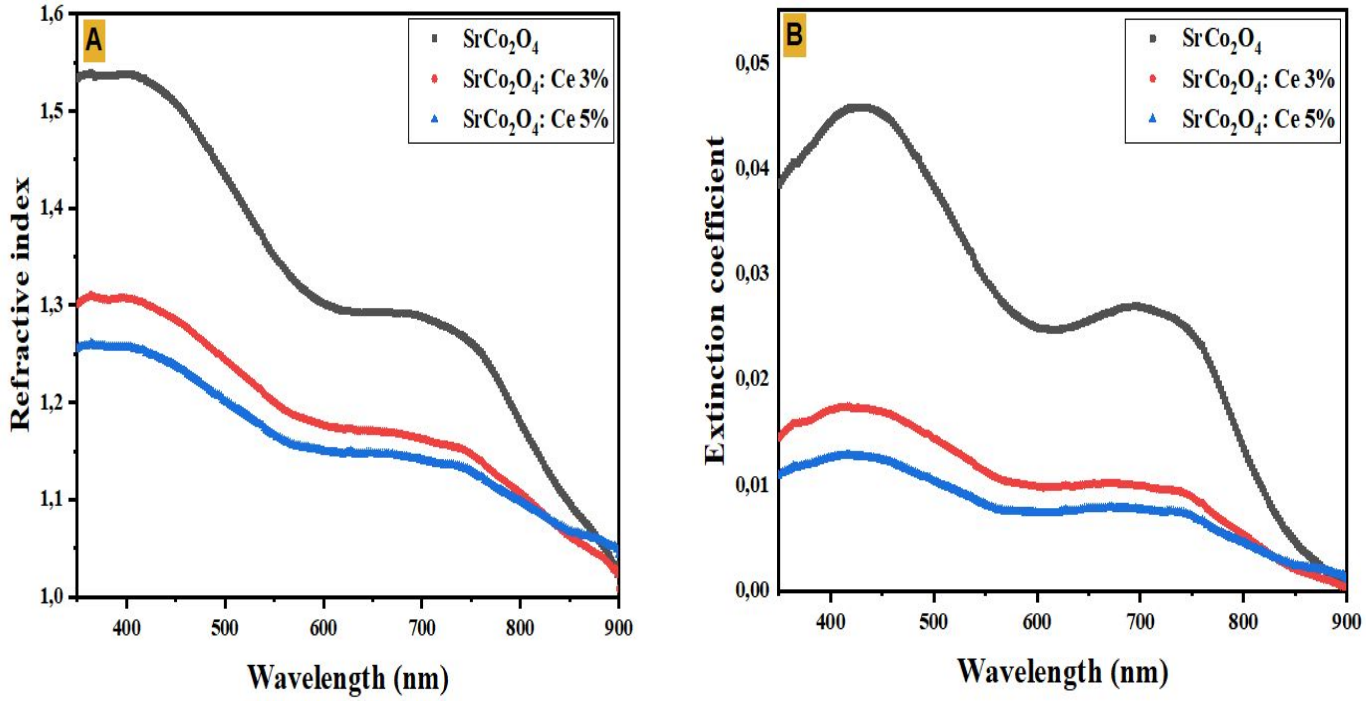

Fig. 8. (A) Refractive index and **(B)** extinction coefficient spectra of pure and Ce-doped $SrCo_2O_4$.

4.3.2. Dielectric Constants:

The polarizability of a solid is directly proportional to its dielectric constant, and its variation with photon energy provides insight into the nature of photon–electron interactions within the films over the investigated energy range.

The materials having a higher value of dielectric constant are enriched with the intrinsic charge carrier[66].The real and imaginary parts of complex dielectric constants mainly depend on the values of n and k, are expressed as[67]:

$$\boldsymbol{\varepsilon_r = n^2 - k^2} \quad \text{..... (11)}$$

$$\boldsymbol{\varepsilon_i = 2nk} \quad \text{..... (12)}$$

Where $\boldsymbol{\varepsilon_r}$ and $\boldsymbol{\varepsilon_i}$ are the real and imaginary parts of the dielectric constant, n is the refractive index and k is the extinction coefficient respectively. The variation of $\boldsymbol{\varepsilon_r}$ and $\boldsymbol{\varepsilon_i}$ values of the samples with photon energy are shown in figure 9 and listed in table 3. It's well observed that the real and imaginary parts follow the same pattern. Since according to the previous relation, $\boldsymbol{\varepsilon_r}$ depends on the square of n (subtraction is negligible), whereas $\boldsymbol{\varepsilon_i}$ is related to multiplication of n and k. For this, the real parts of the dielectric constant are higher than that of the imaginary parts of the dielectric constant [68].

Table 3. The refractive index, extinction coefficient and dielectric constants values of the samples at wavelength of 750 nm.

Samples	Refractive index	Extinction coefficient	Real part of the dielectric constant	Imaginary part of the dielectric constant
Pure $SrCo_2O_4$	1.26	0.024	1.59	0.061
$SrCo_2O_4$: Ce 3%	1.14	0.009	1.31	0.020
$SrCo_2O_4$: Ce 5%	1.12	0.007	1.27	0.016

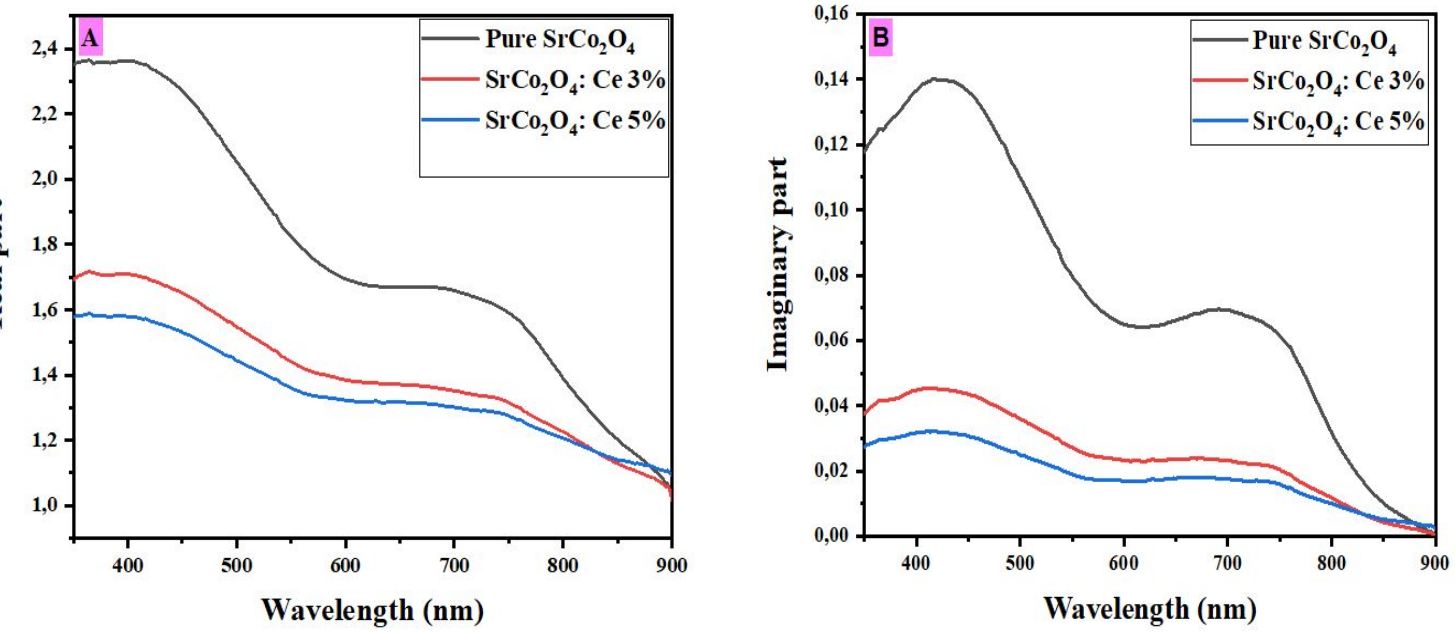

Fig. 9. (A) Variation of real dielectric constant **(B)** imaginary dielectric constant with wavelength of $SrCo_2O_4$ thin films.

4.4. Complex impedance analysis

In order to explain the conduction and polarization processes of the synthesized materials, a complex impedance spectroscopy analysis was conducted in the frequency range of 75 kHz to 20 MHz at room temperature. The Nyquist plots (-Z" vs Z') of the pure and doped $SrCo_2O_4$ is showed in Figure 10. As shown in Figure 5, the complex impedance spectra of the thin films at different doping ratios are all configuration as depressed semicircles. It shows that with increasing doping rate, the semicircle of the Nyquist plot becomes smaller, suggesting that the strength of the material gradually decreased. The literature has shown that the amplitude of the real and imaginary part of the impedance are strongly affected by the resistance[69]. The electrical properties of the material mainly linked to the electrical

properties of the grains and the grain boundaries are described by an equivalent electrical circuit comprising two branches consisting of a parallel connection (RpCp) [70].

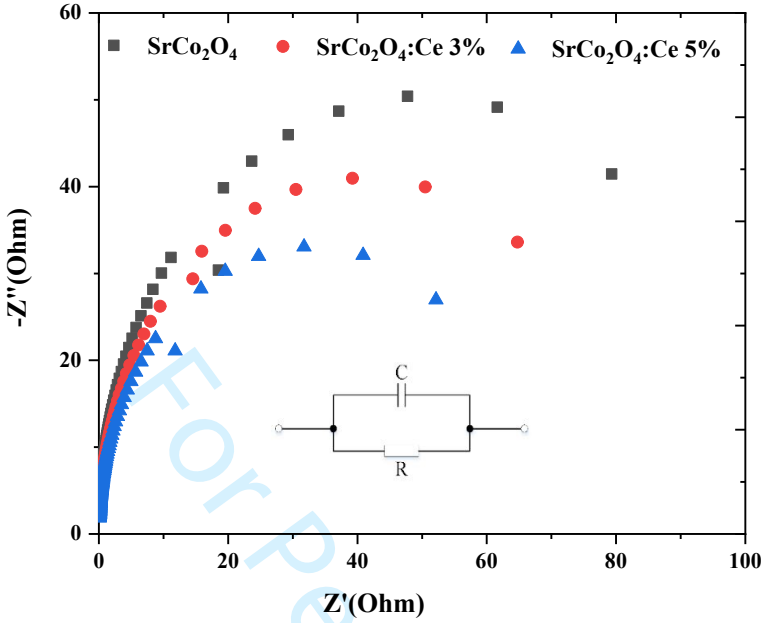

Fig.10. Nyquist plots of undoped and Ce-doped $SrCo_2O_4$ thin films

The diagrams of the films correspond to semicircles whose equation below allows us to reduce the value of the capacity of the grain boundaries of the oxide layer from the Nyquist plots [71]:

$$C_p = \frac{1}{2\pi f_{max} R_p} \quad \text{.....(13)}$$

Where f_{max} is the frequency of the external applied field at the apex of the circular arc. The resistance R_p was determined by the intersection of the Nyquist plot with the real axis.

Table 4: Values of: f_{max}, *Rp*, and *Cp* of and Ce-doped $SrCo_2O_4$ thin Films.

Samples	f_{max} *(KHZ)*	*Rp(Ω)*	*Cp (nF)*
Pure $SrCo_2O_4$	519.44	47.75	6.41
$SrCo_2O_4$:Ce 3%	519.44	40.95	7.13
$SrCo_2O_4$:Ce 5%	519.44	33.06	7.32

The electrical capacitance (C_P) and resistance (R_P) of the pure and doped thin films were calculated from the impedance complex measurement and their variations are graphically represented in Fig.10. The reduction of the bandgap energy has a direct impact on the conductivity of the doped materials thus causing the decrease in resistance. On the other hand, the capacitance increases from 6.41nF to 7.32 nF with Ce doping.

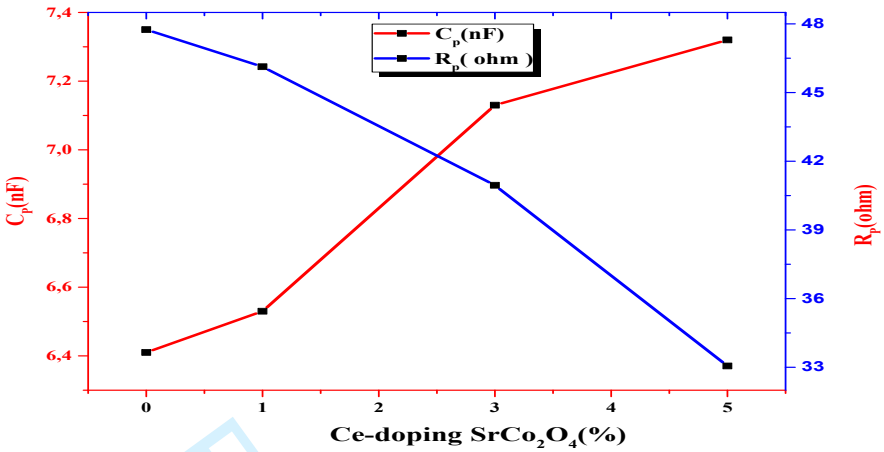

Fig.11. Variation in the resistance and capacitance of thin $SrCo_2O_4$ films as a function of Cerium doping rate.

We notice from Fig 6 and table 4, this shift is also due to the introduction of cerium ions into the $SrCo_2O_4$ lattice, which induces a variation in particle size and consequently introduces more grain boundaries in the samples. Two conduction mechanisms are simultaneously present: conduction through the grains and conduction through the grain boundaries. The effect of the grain boundaries in the samples becomes more dominant compared to the contribution of the grains in the conduction mechanism.

The results obtained suggest that cerium doping is a promising strategy for optimizing Co3O4-based electrode materials for batteries, paving the way for the development of efficient and cost-effective energy storage systems [72-73].

5. Conclusion

Structural, optical, and electrical properties of pure $SrCo_2O_4$ and Ce-doped $SrCo_2O_4$ thin films synthesized using a Dip-coating method with different Cerium concentrations of 0,3% and 5 % are investigated. XRD patterns and IR spectra indicated that Ce ions substituted the Sr ions without altering the material spinel structure. The average nonmetric size of the crystallites increases then begins to decrease with the increase in the doping rate. The films showed highly transparency in the visible region which is favourite for the optoelectronic application in the development of transparent device, and the transmittance increases with the raising. The direct bandgap energy of revealed the $SrCo_2O_4$ thin flms depend strongly on the Co/Ce molar ratio.The complex impedance spectra of the thin films at different doping ratios are all configuration as depressed semicircles.

Acknowledgments

The authors would like to extend their thanks to Prof. El-Habib BELARBI as well as all the members of the Synthesis and Catalysis Laboratory of the Faculty of Material Sciences at the University of Tiaret for all the measurements carried out within the framework of this work.

References

1. Masud, M. H., Nuruzzaman, M., Ahamed, R., Ananno, A. A., & Tomal, A. A. Renewable energy in Bangladesh: current situation and future prospect. Int. J. of. Sustainable. Energy. **39**(2), 132-175(2020).
2. Babalola, A. V., Oluwasusi, V., Owoeye, V. A., Emegha, J. O., Pelemo, D. A., Fasasi, A. Y., ..& Yusuf, S.. Effect of tin concentrations on the elemental and optical properties of zinc oxide thin films. Heliyon. **10**(1) (2024).
3. Manjunatha, K., Angadi, V. J., Ribeiro, R. A., Longo, E., Oliveira, M. C., Bomio, M. R., ... & Pasha, M. (2020). Structural, electronic, vibrational and magnetic properties of Zn^{2+} substituted $MnCr_2O_4$ nanoparticles. Int. J .of. Quant. Chem. 120, e26368 (2020).
4. Kushwaha, A. K. Vibrational, elastic properties and sound velocities of ZnGa2O4 spinel. Computational materials science.85, 259-263(2014).
5. Pisani, L., Maitra, T., & Valentí, R. Effects of Fe substitution on the electronic, transport, and magnetic properties of Zn Ga_2O_4: A systematic ab initio study. Phys B Condens. Matter . **73**(20), 205204(2006).
6. Dixit, H., Tandon, N., Cottenier, S., Saniz, R., Lamoen, D., Partoens, B., ... & Waroquier, M. Electronic structure and band gap of zinc spinel oxides beyond LDA: $ZnAl_2O_4$, $ZnGa_2O_4$ and $ZnIn_2O_4$. New .J. of. Phys. **13**(6), 063002 (2011).
7. Mekprasart, W., Boonyarattanakalin, K., Pecharapa, W., & Ishihara, K. N. Optical characteristics of samarium doped $ZnAl_2O_4$ nanomaterials synthesized by vibrational milling process. Mater. Today: Proce. **5**(6), 14126-14130 (2018).
8. Mansour, A. M., Morsy, M., El Nahrawy, A. M., & Abou Hammad, A. B. Humidity sensing using Zn (1.6− x) Na0. 4CuxTiO_4 spinel nanostructures. Scientific Reports. **14**(1), 562(2024).
9. Lu, Q., Wei, Z., Wu, X., Huang, S., Ding, M., & Ma, J. Electronic structure and optical properties of spinel structure Zn1-xNixAl_2O_4 nanopowders synthesized by sol–gel method. Chemi. Phys.Lett. 772, 138582(2021).
10. Paudel, T. R., Zakutayev, A., Lany, S., d'Avezac, M., & Zunger, A. Doping rules and doping prototypes in A_2BO_4 spinel oxides. Adv. Func .Mater. **21**(23), 4493-4501 (2011).
11. Yousef, R., Nassif, A., Al-Zoubi, A., & Al-Din, N. S. Synthesis and characterisation of structural and electrical properties of $CuMn_2O_4$ spinel compound. Journal of King Faisal University: Basic .and Applied .Sci. **22**(2), 47-50(2021).
12. Vijitha, S. J., Mohanraj, K., & Jebin, R. P. Structural, optical, and surface modifications by varying precursor concentrations on spray deposition of In doped Co_3O_4 thin films for electro chemical application. Chem. Phys. Impact. 6, 100143(2023).
13. Mei, J., Liao, T., Ayoko, G. A., Bell, J., & Sun, Z. Cobalt oxide-based nanoarchitectures for electrochemical energy applications. Prog .in. Mater .Sci. 103, 596-677(2019).
14. Shkir, M., Khan, Z. R., Khan, A., Chandekar, K. V., Sayed, M. A., & AlFaify, S. A comprehensive study on structure, opto-nonlinear and photoluminescence properties of Co3O4 nanostructured thin films: An effect of Gd doping concentrations. Ceram. Int.**48**(10), 14550-14559(2022).
15. Lankauf, K., Cysewska, K., Karczewski, J., Mielewczyk-Gryń, A., Górnicka, K., Cempura, G., ... & Molin, S. (2020). MnxCo_3-xO_4 spinel oxides as efficient oxygen evolution reaction catalysts in alkaline media. Int.J. of hyd. Energy, **45**(29), 14867-14879.
16. Heiba, Z. K., Deyab, M. A., Mohamed, M. B., Farag, N. M., El-Naggar, A. M., & Plaisier, J. R. (2021). Electrochemical performance of $CuCo_2O_4$/CuS nanocomposite as a novel electrode material for supercapacitor. Applied Physics A. 127(11), 853.

17. Li, M., Meng, Z., Feng, R., Zhu, K., Zhao, F., Wang, C., ... & Chu, P. K. Fabrication of bimetallic oxides (MCo_2O_4: M= Cu, Mn) on ordered microchannel electro-conductive plate for high-performance hybrid supercapacitors. Sustainability. **13**(17), 9896(2021).
18. Patel, A. R., Sereda, G., & Banerjee, S. Synthesis, characterization and applications of spinel cobaltite nanomaterials. Current. Pharma. Biotec. **22**(6), 773-792(2021).
19. Ali, F., Khalid, N. R., Tahir, M. B., Nabi, G., Shahzad, K., Ali, A. M., & Kabli, M. R. Capacitive properties of novel Sb-doped Co_3O_4 electrode material synthesized by hydrothermal method. Ceram. Int**.47**(22), 32210-32217(2021).
20. [20] Ali, F., & Khalid, N. R. Facile synthesis and properties of chromium-doped cobalt oxide (Cr-doped Co3O4) nanostructures for supercapacitor applications. Appl. Nanosc. 10(5), 1481-1488(2020).
21. Worku, A. K., Asfaw, A., & Ayele, D. W. (2024). Engineering of Co_3O_4 electrode via Ni and Cu-doping for supercapacitor application. Front. In. Chem. **12** 1357127 (2024).
22. Wen, L., Li, X., Zhang, R., Liang, H., Zhang, Q., Su, C., & Zeng, Y. J. Oxygen vacancy engineering of MOF-derived Zn-doped Co3O4 nanopolyhedrons for enhanced electrochemical nitrogen fixation. ACS. Applied. Mater. & Inter. **13**(12), 14181-14188(2021).
23. Albargi, H., Marnadu, R., Sujithkumar, G., Alkorbi, A. S., Algadi, H., Shkir, M., ... & Sreedevi, G. Deposition of nanostructured Sn doped Co_3O_4 films by a facile nebulizer spray pyrolysis method and fabrication of p-Sn doped Co_3O_4/n-Si junction diodes for opto-nanoelectronics. Sensors. and Actuators. A: Physical.332, 113067(2021)
24. Ghaziani, M. M., Mazloom, J., & Ghodsi, F. EEffect of Mg substitution on the physical and electrochemical properties of Co_3O_4 thin films as electrode material with enhanced cycling stability for pseudocapacitors. J. of .Sol-Gel Sci. and .Tech.**103**(1), 244-257(2022).
25. Khalid, N. R., Batool, A., Ali, F., Nabi, G., Tahir, M. B., & Rafique, M. Electrochemical study of Mo-doped Co_3O_4 nanostructures synthesized by sol–gel method. J. of. Mater.Sci: Mater in Electron.**32**(3), 3512-3521(2021).
26. Manickam, M., Ponnuswamy, V., Sankar, C., Suresh, R., Mariappan, R., Chandra Bose, A., & Chandrasekaran, J. Structural, optical, electrical and electrochemical properties of Fe: Co_3O_4 thin films for supercapacitor applications. J. of Mater. Sci: Mater. In. Electron. **28**(24), 18951-18965 (2017).
27. Xu, Y., Huang, J. C., Cheng, L., Cao, D. X., & Wang, G. L. Ag doped Co_3O_4 nanowire arrays as an electrode material for electrochemical capacitors. Applied Mech. and Mater. 268, 157-163(2013).
28. Ali, F., Khalid, N. R., Nabi, G., Ul-Hamid, A., & Ikram, M. (2021). Hydrothermal synthesis of cerium-doped Co_3O_4 nanoflakes as electrode for supercapacitor application. Int .J. Energy. Res. **45** 1999 (2021).
29. Kim, S., Choi, M., & Park, J. Cerium-doped oxide-based materials for energy and environmental applications. Crystals. **13**(12), 1631(2023).
30. Moumen, A., Kumarage, G. C., & Comini, E. P-type metal oxide semiconductor thin films: Synthesis and chemical sensor applications. Sensors. **22**(4), 1359 (2022).
31. Laouini, E., Hamdani, M., Pereira, M. I. S., Douch, J., Mendonça, M. H., Berghoute, Y., & Singh, R. N. Preparation and electrochemical characterization of spinel type Fe–Co_3O_4 thin film electrodes in alkaline medium. Inter. J. of. Hydr. Energy. **33**(19), 4936-4944 (2008).
32. Venkatesh, R., Dhas, C. R., Sivakumar, R., Dhandayuthapani, T., Sudhagar, P., Sanjeeviraja, C., & Raj, A. M. E. Analysis of optical dispersion parameters and electrochromic properties of manganese-doped Co3O4 dendrite structured thin films. J. of .Phys. and. Chem. Of. Solids. 122, 118-129 (2018).
33. Morán-Lázaro, J. P., López-Urías, F., Muñoz-Sandoval, E., Blanco-Alonso, O., Sanchez-Tizapa, M., Carreon-Alvarez, A., ... & Rodríguez-Betancourtt, V. M. Synthesis, characterization, and sensor applications of spinel $ZnCo_2O_4$ nanoparticles. Sensors. **16**(12), 2162 (2016).

34. Le Trong, H., Bui, T. M. A., Presmanes, L., Barnabé, A., Pasquet, I., Bonningue, C., & Tailhades, P. Preparation of iron cobaltite thin films by RF magnetron sputtering. Thin Solid Films. 589, 292-297 (2015).
35. Katayama, T., Mo, S., Kurauchi, Y., Chikamatsu, A., & Hasegawa, T. Synthesis and magnetism of $MoCo_2O_4$ spinel thin films. Thin Solid Films, 728, 138696(2021).
36. Lakehal, A., Bedhiaf, B., Bouaza, A., Hadj, B., Ammari, A., & Dalache, C. Structural, optical and electrical properties of Ni-doped Co3O4 prepared via Sol-Gel technique. Mater. Res, **21**(3), e20170545(2018).
37. Dalache, C., Benhebal, H., Benrabah, B., Ammari, A., Kharroubi, A., & Lakhal, A. Cadmium-doped Co_3O_4 thin films: synthesis and characterization. Surface Review and Letters.**26**(01), 1850134(2019).
38. Barrera, C. E., Martinez-Flores, J., Gonzalez, G., Ortega-Lopez, M., & Rosas, R. Spectroscopic ellipsometry study of Co_3O_4 thin films deposited on several metal substrates. The Open .Surf. Sci.J. **5**(1), 9-16(2013).
39. Faustini, M., Louis, B., Albouy, P. A., Kuemmel, M., & Grosso, DPreparation of sol− gel films by dip-coating in extreme conditions. The .J. of Phys. Chem. C**, 114**(17), 7637-7645 (2010).
40. Butt, M. A. Thin-film coating methods: a successful marriage of high-quality and cost-effectiveness—a brief exploration. Coatings, **12**(8), 1115(2022).
41. Simonenko T.L., Simonenko N.P., Gorobtsov P.Y. et al. Pen plotter printing of Co_3O_4 thin films: features of the microstructure, optical, electrophysical and gas-sensing properties. J. Alloy. Compd. 832,154957(2020).
42. M. Mahinzad Ghaziani, J. Mazloom and F. E. Ghodsi., Effect of Mg substitution on the physical and electrochemical properties of Co_3O_4 thin films as electrode material with enhanced cycling stability for pseudocapacitors. J. of .Sol-Gel Sci. and Techn103,244–257(2022).
43. Al-Senani, G. M., Deraz, N. M., & Abd-Elkader, O. H. Magnetic and characterization studies of CoO/Co_3O_4 nanocomposite. Processes, **8**(7), 844 (2020).
44. Shinde, S. K., Yadav, H. M., Ramesh, S., Bathula, C., Maile, N., Ghodake, G. S., ... & Kim, D. Y. High-performance symmetric supercapacitor; nanoflower-like NiCo2O4//NiCo2O4 thin films synthesized by simple and highly stable chemical method. J Mol Liq 299:112119. (2020).
45. Kayani, Z. N., Arshad, S., Riaz, S., & Naseem, S. Investigation of structural, optical and magnetic characteristics of Co3O4 thin films. Applied Physics A. **125**(3), 196(2019).
46. Manickam, M., Ponnuswamy, V., Sankar, C., & Suresh, R. Cobalt oxide thin films prepared by NSP technique: Impact of molar concentration on the structural, optical, morphological and electrical properties. Optik, **127**(13), 5278-5284 (2016).
47. Aghazadeh, MElectrochemical preparation and properties of nanostructured Co_3O_4 as supercapacitor material. J. of .Applied. Electroch.**42**(2), 89-94(2012).
48. UmaSudharshini, A., Bououdina, M., Venkateshwarlu, M., Dhamodharan, P., & Manoharan, C. Solvothermal synthesis of Cu-doped Co_3O_4 nanosheets at low reaction temperature for potential supercapacitor applications. Applied Physics A. 127(5), 353 (2021).
49. Naveen, A. N., & Selladurai, S. Investigation on physiochemical properties of Mn substituted spinel cobalt oxide for supercapacitor applications. Electroc. Acta. 125, 404-414(2014).
50. Faraj, M. G., & Esia, M. H. Effect of polyimide substrate on the physical properties of Aluminum doped Zinc Oxide (AZO) thin films deposited by spray pyrolysis technique. Digest .J. of. Nanomater. and Biostr. 14, 471-478(2019).
51. Boudjouan, F., Chelouche, A., Touam, T., Djouadi, D., Mahiou, R., Chadeyron, G., ... & Boudrioua, A. Doping effect investigation of Li-doped nanostructured ZnO thin films prepared by sol–gel process. J. of .Mater. Sci: Mater in Electro. **27**(8), 8040-8046(2016).
52. Özpolat, Y., Algün, G., Akçay, N., & İldeş, C. Effect of cerium doping on enhanced UV-shielding capacity of nanostructured ZnO thin films. J. of .Mater. Sci: Mater in Electro. **36**(16), 989(2025).

53. Ahmet Güngör., Enhanced supercapacitor performance with cerium-doped polypyrrole nanofibers. J. Mater. Chem. A , **13**, 18641(2025).
54. Kayani, Z. N., Chaudhry, W., Sagheer, R., Riaz, S., & Naseem, S. Effect of Ce doping on crystallite size, band gap, dielectric and antibacterial properties of photocatalyst copper oxide Nano-structured thin films. Mater. Sci and Engin : B **283**,115799(2022).
55. Ahmed, A. S., Singla, M. L., Tabassum, S., Naqvi, A. H., & Azam, A. Band gap narrowing and fluorescence properties of nickel doped SnO2 nanoparticles. J. of . Lumin, **131**(1), 1-6. (2011).
56. Najm, A. S., Aljuhani, A., Naeem, H. S., Sopian, K., Ismail, R. A., Holi, A. M., ... & Moria, H. Mechanism and principle of doping: realizing of silver incorporation in CdS thin film via doping concentration effect. RSC advances, **12**(46), 29613-29626(2022).
57. Bangi, U. K. M. Impact of cadmium salt concentration on CdS nanoparticles synthesized by chemical precipitation method. Chalcogenide Letters, 17(11), 537-547. (2020).
58. Ikhmayies, S. J., & Ahmad-Bitar, R. N. Temperature dependence of the photoluminescence spectra of CdS: In thin films prepared by the spray pyrolysis technique. J.of .Lumin, 142, 40-47(2013).
59. Khatibani, A. B., & Rozati, S. M. Optical and morphological investigation of aluminium and nickel oxide composite films deposited by spray pyrolysis method as a basis of solar thermal absorber. Bul. of Mater.Sci. 38(2), 319-326(2015).
60. Boucherka, T., Brihi, N., Berbadj, A., & Touati, M. Effect of indium doping on the UV photoluminescence emission, structural, electrical and optical properties of spin-coating deposited SnO_2 thin films. Optik,209, 64586 (2020).
61. Hameed, T. A., Wassel, A. R., & El Radaf, I. MInvestigating the effect of thickness on the structural, morphological, optical and electrical properties of $AgBiSe_2$ thin films. J. of. Alloys. And. Compd.805, 1–11. (2019).
62. Madhuri, K. V., & Babu, M. BStudies on electron beam evaporated WO_3 thin films. Materials Today: Proceedings.**3**(1), 84–89. (2016).
63. Mahjabin, S., Haque, M. M., Sobayel, K., Selvanathan, V., Jamal, M. S., Bashar, M. S., Sultana, M., Hossain, M. I., Shahiduzzaman, M., Algethami, M., Alharthi, S. S., Amin, N., Sopian, K., & Akhtaruzzaman, MInvestigation of morphological, optical, and dielectric properties of RF sputtered WO_x thin films for optoelectronic applications. Nanomaterials. **12**(19), 3467. (2022).
64. Roguai, S., & Djelloul, A. Structural, morphological, optical and electrical properties of Ni-doped SnO2 thin films by pneumatic spray pyrolysis method. Bull.of. Mater. Sci. **45**(4), 227 (2022).
65. Ahmed, M. T., Islam, S., Bashar, M. S., Hossain, M. A., & Ahmed, F. Synthesis and characterizations of CH3NH3PbI3: ZnS microrods for optoelectronic applications. Advan in Mater Scie.and. Engin, **2022**(1), 7606339(2022).
66. Li, W., Zhao, K., Zhou, H., Yu, W., Zhu, J., Hu, Z., & Chu, J. Precursor solution temperature dependence of the optical constants, band gap and Urbach tail in organic–inorganic hybrid halide perovskite films. J. of .Physics D: Applied Physics. **52**(4), 045103(2019).
67. Suresh, R., Ponnuswamy, V., & Mariappan, R. Influence of mole concentration on the optical properties of nebulized spray coated CeO_2 thin films. J. of .Optics, 44, 203–209(2015).
68. Bagheri Khatibani, A., & Rozati, S. M. Optical and morphological investigation of aluminium and nickel oxide composite films deposited by spray pyrolysis method as a basis of solar thermal absorber. Bull. of .Mater.Sci . 38, 319–326(2015).
69. Sinclair, D. C., & West, A. R. Impedance and modulus spectroscopy of semiconducting BaTiO3 showing positive temperature coefficient of resistance. Journal of Applied Physics, **66**(8), 3850-3856(1989).
70. Bisht, G. S., & Pal, D. Correlation between magnetic and dielectric anomalies arising due to spin-chain arrangements in the paramagnetic phase of 1D Ca3Co1. 9Bi0. 1O6. In Journal of Physics: Conference Series. (1) 2518, 012001 (2023).

71. Abdelmalek Kharroubi, Aboulkacem., Khiali, Hadj Benhebal., Bedhiaf Benrabah., Salima Lellou., Samir Kadi and Bellal Sadouki.Synthesis and Properties of (Bi, Cd)-doped $CuMn_2O_4$ thin films by sol-gel dip-coating method »Physics and Chemistry of Solid State, **22**, 4 734-741(2021).
72. El-Habib, A,Oubakalla, M.Haloui, S, Nejmi, Y,El Bouji, M, Yousfi, A,El Mansouri, F, Aouni, A, Diani, M, Addou, M. Investigating the Influence of Cerium Doping on the Structural, Optical, and Electrical Properties of $ZnCexCo_{2-x}O_4$ Zinc Cobaltite Thin Films. Crystals **15**, 742(2025).
73. Pitcheri, R., Mooni, S. P, Radhalayam, D, Nora, M, Roy, S, Al-Zahrani, F. A. M., & Suneetha, M. Effect of Ce-doping on the structural, morphological, and electrochemical features of Co_3O_4 nanoparticles synthesized by solution combustion method for battery-type supercapacitors. Ceram Inter, **50**(23), 50504-50515(2024).

Table .1. Structural parameters as crystalline size, lattice parameter, cell volume, micro strain and dislocation density of $SrCo_2O_4$ and Ce-doped $SrCo_2O_4$

Sample	**Undoped $SrCo_2O_4$**	**$SrCo_2O_4$:Ce 3%**	**$SrCo_2O_4$:Ce 5%**
β	0,0061928	0,0055822	0,0052333
θ	18,305	18,42	18,44
cos θ	0,949398	0,94876577	0,9486554
sinθ	0,314075	0,31598023	0,3163114
Average crystallite size D (nm)	23,58	26,18	27,93
d_{hkl} (Å)	2,453	2,438	2,435
Lattice constant a (Å)	8,136	8,086	8,076
Unit cell volume V_{cell} $(Å)^3$	538,56	528,69	526,73
Dislocation density δ (lines/m^2)	17,98 10^{14}	14,59 10^{14}	13,42 10^{14}
Microstrain ε (line^{-2} m^{-4})	0,0014698	0,0013240	0,0012411

Table 2: The optical band gap and Urbach energy for the undoped and Ce-doped $SrCo_2O_4$ thin films.

Ce content at. %	Bandgap (eV)		Urbach energy (meV)	
	E_{g1} (eV)	E_{g2} (eV)	E_{u1} (meV)	E_{u2} (meV)
0	1,48	1.76	48	697
3	1,44	1.71	70	704
5	1,40	1.70	150	753

Table 3. The refractive index, extinction coefficient and dielectric constants values of the samples at wavelength of 750 nm.

Samples	Refractive index	Extinction coefficient	Real part of the dielectric constant	Imaginary part of the dielectric constant
Pure $SrCo_2O_4$	1.26	0.024	1.59	0.061
$SrCo_2O_4$: Ce 3%	1.14	0.009	1.31	0.020
$SrCo_2O_4$: Ce 5%	1.12	0.007	1.27	0.016

Table 4: Values of: f_{max}, *Rp*, and *Cp* of and Ce-doped $SrCo_2O_4$ thin Films.

Samples	f_{max} *(KHZ)*	*Rp(Ω)*	*Cp (nF)*
Pure $SrCo_2O_4$	519.44	47.75	6.41
$SrCo_2O_4$:Ce 3%	519.44	40.95	7.13
$SrCo_2O_4$:Ce 5%	519.44	33.06	7.32